Development of a Biomimetic Peptide-Based Nanoformulation Against the Breast Cancer

Parichehr Hassanzadeh[1,2], Elham Arbabi[3], Fatemeh Rostami[3]

[1] *Nanotechnology Research Center, School of Pharmacy, Tehran University of Medical Sciences, Tehran, Iran*

[2] *Sasan Hospital, Tehran, Iran*

[3] *Research Center for Gastroenterology and Liver Diseases, Shahid Beheshti University of Medical Sciences, Tehran, Iran*

Received: 03 Jan. 2021; Accepted: 12 Jun. 2021

Abstract- Nanotechnology has enabled the preparation of various materials for overcoming the rapid clearance of drugs, nonspecific uptake or actions, and poor tumor penetration. Based on the significance of using biomimetic substances, silk fibroin nanoparticles (SF-NPs) have been increasingly prepared for the delivery of therapeutics. Meanwhile, aggregation and low stability in the biological medium may negatively affect their efficiency. This prompted us to coat SF-NPs with polydopamine (PDA), and for efficient accumulation and increasing therapeutic efficiency against breast cancer, paclitaxel (PTX)-loaded PDA-coated SF-NPs were conjugated with targeting peptide, iRGD (iRGD-PDA-PTX-SF-NPs). The peptide impacts on the cellular uptake, cytotoxicity, tumor penetrability of NPs, and their antitumor effects were evaluated. iRGD-PDA-PTX-SF-NPs with suitable physicochemical characteristics and drug loading released PTX in a controlled manner, and efficient cellular uptake was observed. Improved pharmacological profile of PTX was revealed by increased anticancer effects *in vitro* and in tumor-bearing Balb/c mice, including the delayed growth of the tumor and enhanced rate of survival. The prepared NPs showed no toxic effects against the healthy tissues indicating the histocompatibility and safety of these biomimetic and long-circulating nanoplatforms. The peptide-based SF-NPs could be considered as promising biomimetic nanoformulation against breast cancer.

Acta Med Iran 2021;59(7):430-441.

Keywords: Breast cancer; Silk fibroin; Polydopamine; Internalizing arginine-glycine-aspartic acid (iRGD); Paclitaxel; Balb/c mice

Introduction

Breast cancer, an aggressive and heterogeneous disease with various clinical symptoms, is one of the most common causes of death in women worldwide (1). Besides the non-durable effects and remarkable side effects, conventional treatment approaches such as the chemo- and radio-therapies or surgery may be associated with a variety of complications, including the high rates of relapse or metastasis due to the low drug bioavailability or repressing the anti-metastatic immunity leading to the poor prognosis and reduced patient's quality of life (2-4). Drug resistance is another obstacle against effective cancer therapy (5). As known, exposure of drug-resistant breast cancer cells to high-dose anticancer agents may result in cell death (6). In cell culture, drug-resistant breast tumorspheres have been destroyed. Meanwhile, toxicities associated with such high doses can negatively affect the efficiency of therapeutics (7). Application of the monoclonal antibodies has been represented as a promising treatment strategy. However, they may be associated with various limitations, such as low penetration into the tumors because of their large size, nonspecific uptake, or resistance (8-10). Over the last decades, increasing nanotechnology-based research efforts have been made to develop more effective and safer anticancer therapeutics (11,12). The application of drug-conjugated

Corresponding Author: P. Hassanzadeh
Nanotechnology Research Center, School of Pharmacy, Tehran University of Medical Sciences, Tehran, Iran
Tel: +98 2166959095, Fax: +98 2166581558, E-mail address: hassanzadehparichehr4@gmail.com

nanoparticles (NPs) for systemic and targeted delivery has led to the improved stability and pharmacological profiles of therapeutics agents (13,14). Biodegradable NPs produced from synthetic or natural biomaterials have been represented as stable and scalable drug delivery systems (15,16). Because of the suitable physical and mechanical characteristics, biodegradability, and biocompatibility, silk-based materials have been extensively used for a variety of biomedical applications, including cancer therapy (17,18). Using appropriate techniques enables silk processing into various structures, including the scaffolds, microcapsules, films, nano- or microspheres, and hydrogels (19,20). Silk fibroin (SF), a biodegradable and biocompatible natural protein with low immunogenicity and capable of creating useful tissue constructs, can be used for the controlled release of drugs (21,22). Using SF rods or NPs has enabled long-term and loco-regional delivery of therapeutics against breast cancer (23,24). Doxorubicin entrapped in SF-NPs has been more effective than free drug against the *in vitro* model of breast cancer and overcome drug resistance (25). Methotrexate-loaded SF-albumin NPs have demonstrated selective killing of MDA-MB-231 breast cancer cells (26). In primary breast cancer, doxorubicin-loaded SF hydrogels have improved treatment efficiency and safety as compared to the systemic administration of doxorubicin (27). This prompted us to encapsulate the widely-applied anticancer drug paclitaxel (PTX) into the SF-NPs as poor solubility of PTX, and nonspecific body distribution that might result in the inappropriate tumor penetration and toxic effects against the healthy organs (28,29) may negatively affect its efficiency. Furthermore, limiting dose or dosage frequency can result in the resistance of cancer cells. Furthermore, we have coated SF-NPs in order to minimize the risks of aggregation or poor stability of this type of NPs in the biological media (30,31). Coating NPs with polyethylene glycol (PEG) has been associated with a number of limitations, such as rapid blood clearance and significantly reduced plasma concentrations even after repeated injections of the nanoformulations (32,33). In addition, the accumulation of the PEGylated NPs can negatively affect their efficiency or enhance side effects (34,35). Besides very good cytocompatibility and capability of gatekeeping and immobilizing the biomolecules, polydopamine (PDA) coating has been shown to attenuate unwanted immune responses (36,37). Simple structure, functional groups which facilitate interactions with a variety of inorganic or organic substrates, and cost-effectiveness are other beneficial aspects of PDA (38,39). The efficient grafting of PDA-coated materials with various enzymes, polysaccharides, antibodies, anticancer therapeutics, growth factors, and peptides has also been well-established (39,40). Over the last decade, peptides with low immunogenicity and capable of mimicking the natural proteins have been used for surface decoration of NPs for targeted therapy and overcoming the limitations associated with conventional therapeutics. Because of their suitable stability, tissue penetrability, and little immunogenicity, peptides are suitable alternatives for monoclonal antibodies (41,42). Peptide-based NPs have shown higher biocompatibility than inorganic NPs or synthetic polymers (43,44). Moreover, the application of tumor penetrating peptides for the delivery of drugs enables overcoming drug resistance (45). Internalizing arginine-glycine-aspartic acid (iRGD) is a peptide with high specificity towards $\alpha_v\beta_3$ and $\alpha_v\beta_5$ integrins, which are overexpressed on the endothelial cells of tumors (46). This peptide expands more extensively than other types of RGD peptides into the extravascular tumor tissues and facilitates drug penetration and accumulation into the tumor vessels (47). This prompted us to conjugate iRGD to PDA-coated PTX-loaded SF-NPs in order to provide biocompatible nanocarriers for improving the efficiency of the entrapped drug and reducing its adverse effects.

Materials and Methods

Materials

Paclitaxel, 3-[4,5-dimethylthiazol-2-yl]-2,5-diphenyltetrazolium bromide (MTT), phosphate-buffered saline (PBS), isopropanol, xylazine, ketamine, dimethyl sulfoxide (DMSO), and fluorescein isothiocyanate (FITC) were obtained from Sigma-Aldrich, Germany. MDA-MB-231 cell line was purchased from Pasteur Institute, Tehran, Iran. Cell culture materials were obtained from GIBCO/Invitrogen, Germany.

Methods

SF extraction

Extraction of SF from Bombyx mori cocoons was performed as previously described (48) with some modifications. Following cutting the cocoons and degumming twice in the boiled Na_2CO_3 (0.5%) for 35 min, washing with double-distilled water, air-drying, and dissolving degummed SF in H_2O/ CH_3CH_2OH/ $CaCl_2$ (8:2:1) for 4.5 h at 75° C, the solution was

dialyzed against the deionized water for 72 h using a dialysis bag (MWCO of 10 kDa), centrifuged at 12000 rpm for 25 min, and filtered with 0.22 μm-filter.

Preparation of PTX-loaded SF-NPs (PTX-SF-NPs)

PTX (5 mg in ethanol) was added dropwise to SF solution (5 mg/ml) under stirring followed by filtering, centrifugation at 12000 rpm for 30 min, washing the sediment twice with deionized water, and re-suspending in PBS for 3 s at 30% amplitude by the ultrasound processor (Sonics Vibracell VCX130, US).

Assessment of the entrapment efficiency and the capacity of drug loading:

The capacity of drug loading and entrapment efficiency of PTX-SF-NPs were evaluated using Agilent HPLC system (Agilent Technologies, USA) with C18 column, mobile phase including the water/acetonitrile (48:52, v/v), sample injection of 50 μl, the flow rate of 1 ml/min, and detection wavelength of 227 nm. The limits of detection and quantification were 1.4 and 3.5 μg/ml, respectively.

Entrapment efficiency and the capacity of drug loading were determined as follows:

EE% = [drug amount encapsulated in NPs / total drug amount] × 100

DL% = [drug amount encapsulated in NPs / weight of NPs] × 100

PDA coating on the surface of PTX-SF-NPs (PDA-PTX-SF-NPs)

Surface modifying by PDA was performed as previously described (49). Briefly, 50 mg of PTX- SF-NPs were dispersed in 10 mM Tris–HCl buffer (50 ml, pH 8.5) followed by addition of dopamine hydrochloride (0.5 mg/ml), stirring of the mixture for four h at 22° C, centrifugation for 15 min at 13,000 rpm, and washing of NPs for removing the unattached dopamine.

Preparation and conjugation of targeting peptide to PDA-PTX-SF-NPs

The peptide, iRGD, was synthesized using the fluoromethoxycarbonyl (Fmoc)-based solid-phase strategy as previously described in detail (50,51). iRGD was cyclized through disulfide bridge via resin-bound peptide treatment with thallium trifluoroacetate solution (in *N*, *N*′-dimethylformamide). Peptide cleavage from the resin was performed via application of the trifluoroacetic acid/triisopropylsilane/H_2O (95/2.5/2.5) mixture (52). Mass spectrometry was applied to confirm the formation of the disulfide bond. Peptide purification was evaluated by HPLC. The peptide was conjugated to PDA-PTX-SF-NPs via a Michael-addition reaction. In brief, NPs were suspended in 10 mM Tris buffer (pH 8.5) containing 2 mg/ml of iRGD followed by incubation under stirring for 45 min at 22° C, centrifuging NPs, washing three times, and freeze-drying (53).

NP characterization

Determination of the particle size, polydispersity index (PDI), surface charge, and morphology

Photon correlation spectroscopy (Malvern Instruments, UK) was used for evaluating the size, PDI, and zeta potential of NPs (n=3). The shape and morphology of NPs were assessed by scanning electron microscopy (SEM) (JSM-T20, Japan) following the sample mounting on the aluminum stubs coated with palladium/gold and observing at 25 kV.

Assessment of the fourier transform infrared spectrophotometer (FTIR) spectra

Structural alterations of SF-NPs following drug loading, PDA-coating, and peptide conjugation were evaluated using Fourier transform infrared (FTIR) spectrometer (Bruker, Germany).

Evaluation of the *in vitro* release profile

The release pattern of PTX from SF-NPs was evaluated by dialysis-based method (54) at pH 6 and 7.4. Following suspending of NPs in 1 ml of PBS in the dialysis bag (with 14 kDa MWCO) and immersing in 25 ml of PBS at 37° C under magnetic stirring (100 rpm), 500-μl samples were collected at determined time intervals (maintaining sink condition), and the released amount of PTX was assessed by HPLC as aforementioned. The percentage of drug release was plotted against time, and PTX solution was considered as a control (n=3).

Cell culture

Human breast cancer MDA-MB-231 cells were cultured in the flasks and kept in the humidified incubator (5% CO_2) at 37° C with DMEM supplemented with FBS (10%), 100 U/ml of penicillin G, 100 μg/ml of streptomycin, and 0.25 μg/ml of amphotericin B.

Assessment of the cellular uptake

100 mg of FITC was dissolved in 10 ml of DMSO, added to SF-NPs, and remained for 12 h at 22° C in the dark followed by precipitation of the labeled NPs by 0.5 mM of NaOH, dialysis against the water for 72 h, cell

adhesion, medium removal and cell incubation with samples (100 µg/ml) for five h, three times sample washing with PBS, incubation for 8 min with DAPI, washing three times with PBS, fixing the cells with formaldehyde (1%) for 15 min at 4° C, and evaluation of the cellular uptake using the confocal fluorescence scanning microscope (Nikon, Switzerland). Flow cytometry analysis was performed for quantitative evaluation of the cellular uptake of non-targeted and targeted SF-NPs.

Evaluation of the cytotoxicity *in vitro*

After seeding of MDA-MB-231 cells in 96-well plates (1×10^4/well) and remaining overnight, cells were exposed to free PTX (0.2, 0.5, and 1 µM) (55), iRGD (100 µM) (56), PDA, blank SF-NPs, PTX-SF-NPs (with equivalent PTX concentrations), and iRGD-PDA-PTX SF-NPs (with equivalent PTX concentrations) for 24 h followed by incubating with 20 µl MTT (5 mg/ml) for four h, medium aspiration and replacement by DMSO (100 µl) and 10-min oscillation for the complete dissolving of formazan crystals, and absorbance determination at 570 nm by a microplate reader (Anthos 2020, Austria), (57). Cell viability was demonstrated as a percentage of the untreated cells (as negative control) and presented as mean±SEM (n=3).

***In vivo* studies**

Animals

Female Balb/c mice weighing 15±2 g from Pasteur Institute (Tehran, Iran) were housed under the standard conditions with 12 h dark/light cycle and *ad libitum* access to water and food. All animal experiments have complied with ARRIVE guidelines and are carried out in accordance with the National Institutes of Health guide for the care and use of laboratory animals (NIH Publications No. 8023, revised 1978).

Induction of breast tumor

Following trypsinization of MDA-MB-231 cells with EDTA (0.25%) and pellet collecting via centrifugation for 5 min at 1000 rpm and cell re-suspending with RMPI-1640 medium, 100 µL of cell suspension was subcutaneously inoculated into the right flank of the animal. Tumor-bearing animals were maintained under the standard conditions for further experimental procedures.

***In vivo* imaging**

Targeted and non-targeted SF-NPs were FTIC-labeled as aforementioned (section 2.3.1). Upon reaching the tumor volume to about 100 mm^3 which was measured by a caliper and calculated as follows; volume (mm^3)=($d^2\times D$)/2, (d and D: the smallest and largest diameters of the tumor, respectively), randomly-assigned tumor-bearing animals received tail vein injections of targeted and non-targeted nanoformulations. Perkin-Elmer IVIS spectrum imaging system (USA) was used for image capturing three h after the injection.

Evaluating the penetration of targeted or non-targeted SF-NPs into the tumor tissue

Tumors were harvested for 1, 2, and 3 h followed by fixation in paraformaldehyde (4%) at 4° C overnight, cryoprotection in the sucrose (30%), freezing in the embedment medium, providing 5- mm sections, rehydration of the sections in PBS for 15 min, incubating with BSA (3%) for one h, exposing to the rat anti-mouse CD31 marker for one h, three-time washing the slides with PBS, staining with Alexa Fluor 594 secondary antibody for 45 min in the dark, mounting the slides by Fluoromount aqueous mounting medium, and observing by the confocal microscope (Zeiss, Germany).

Therapeutic potential of NPs against the breast tumor

Upon reaching the tumor volume to about 100 mm^3, animals were randomly divided into six groups and received tail vein injections of vehicle, SF-NPs, iRGD, PTX (1, 2.5, and 5 mg/kg), PTX-loaded SF-NPs (containing the equivalent concentrations of PTX), or iRGD-PDA-PTX SF-NPs (containing the equivalent concentrations of PTX) every four days for seven times (n=10/group). Following regular monitoring of the bodyweight alterations, tumor volumes, and survival rates, three randomly selected mice in each group were sacrificed 30 days after the last treatment followed by collecting the tumor, liver, spleen, kidney, and heart, fixation with paraformaldehyde (4%), paraffin embedment, providing 5-µm sections, mounting on the slides, and staining with hematoxylin and eosin for evaluation of the morphological alterations by microscope (n=3).

Statistical analysis

Shapiro-Wilk test was applied for verifying the normal distribution of data. Analysis of variance (ANOVA) followed by Tukey's test was used for data analysis. Statistical significance in the survival evaluation (plotted as Kaplan-Meier curves) was evaluated by log-rank test. Data have been presented as

mean±SEM, and $P<0.05$ was considered statistically significant.

Results

Characterization of NPs

SF-NPs demonstrated a mean diameter of 113.5±4.6 nm with PDI and ZP of 0.15±0.07 and -29.3±2.7 mV, respectively. PTX-SF-NPs, PDA-PTX-SF-NPs, and iRGD-PDA-PTX-SF-NPs showed diameters of 132.3±3.9, 155.7±6.5, and 171.3±5.7 nm, PDI values of 0.14±0.05, 0.19±0.03, and 0.22±0.07, and ZP values of -28.3±3.7, -25.7±1.9, and -22.5±2.3 mV, respectively, Conjugation of the peptide did not significantly affect the physicochemical properties of SF-NPs. DL% and EE% were 12.3±0.27 and 82.7±3.9, respectively. The morphological assessment revealed the spherical shapes of SF-NPs (Figure 1A). This type of shape was preserved after PTX loading (Figure 1B) or PDA coating and peptide conjugation (Figure 1C).

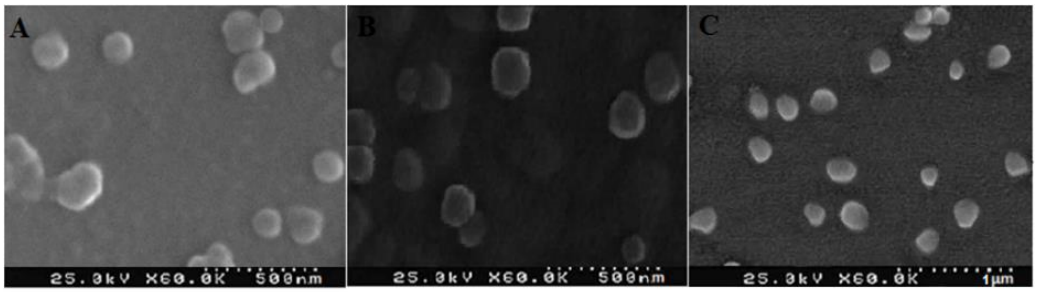

Figure 1. SEM images of SF-NPs (A), PTX-loaded SF-NPs (B), and iRGD-PDA-PTX SF-NPs (C). There is no aggregation between the spheroidal NPs. (PTX: paclitaxel, PDA: polydopamine, SF-NPs: silk fibroin nanoparticles)

FTIR was applied for evaluating the structural alterations of SF-NPs following drug loading, PDA coating, and peptide conjugation (Figure 2). Regarding SF-NPs, peaks corresponding to amide I, II, and III, were observed at 1632, 1525, and 1233 cm^{-1}, respectively. In PTX-loaded SF-NPs, peaks attributed to amide I and II were enhanced to 1653 and 1542 $cm^{-1,}$ and additional peaks at 1254 and 706 cm^{-1} were also observed. Following PDA coating and iRGD conjugation, peaks corresponding to amide I and II were increased to 1659, and 1547 and peaks related to PDA and cyclic aromatic motif of iRGD were also observed.

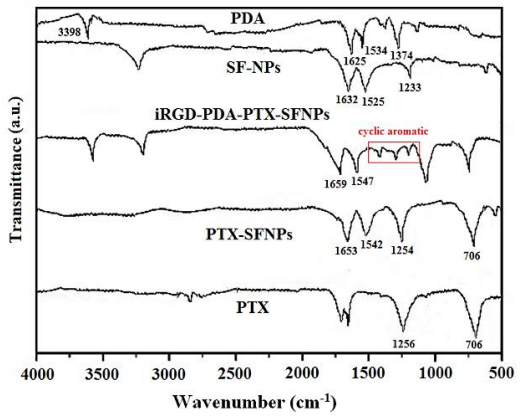

Figure 2. Characterization of NPs by FTIR spectroscopy. In PTX-loaded SF-NPs, peaks attributed to amide I and II were enhanced, and additional peaks were observed, indicating successful drug loading

Characterizing iRGD by ESI-MS spectrum and HPLC

Electrospray ionization mass spectrum (Figure 3A) confirmed the formation of the intra-molecular disulfide bond. m/z observed for [M+H]+ was 1441.8 that was in good agreement with the calculated mass (1441.5). Based on the HPLC profile, the peptide with a purity of about 98% showed a retention time of about 8.6 min (Figure 3 B).

Drug release pattern *in vitro*

PTX release from solution was more rapid than targeted PTX-SF-NPs (Figure 4). There was no remarkable difference between the kinetics of PTX release at physiological and acidic pH (Figure 4, $P>0.05$).

Cellular uptake of the non-targeted and targeted SF-NPs

A significantly higher fluorescence was observed after incubation of MDA-MB-231 breast cancer cells with targeted SF-NPs as compared to the non-targeted ones (Figure 5A and 5B, respectively). These findings were in good agreement with the quantitative measurements of flow cytometry, demonstrating higher intra-cellular fluorescence intensity in the group treated with targeted SF-NPs (Figure 5C) as compared to the non-targeted ones (Figure 5D).

Evaluation of the cytotoxicity *in vitro*

MTT assay was applied for assessment of the *in vitro* toxicity of free PTX, SF-NPs, PDA, iRGD, and non-targeted and targeted SF-NPs (Figure 6). SF-NPs, PDA, and iRGD alone did not show toxic effects against MDA-MB-231 cancer cells. Free PTX and PTX-SF-NPs demonstrated cytotoxic effects only at the highest dose of PTX, while targeted SF-NPs (iRGD-PDA-PTX-SF-NPs) exhibited cytotoxic effects at all doses tested including the lower ones (Figure 6).

***In vivo* imaging**

High fluorescent intensity was observed three h after i.v. injection of targeted SF-NPs (Figure 7). Non-targeted NPs demonstrated lower fluorescent intensities throughout the body. Distribution and tumor penetration of NPs were observed in a time-dependent manner. Targeted NPs (the bottom line in Figure 7) moved away from the blood vessels (in red) towards the tumor tissue. At three h post-injection, more targeted SF-NPs left the blood vessels and deeply penetrated into the tumor tissue, while non-targeted NPs (the upper line in Figure 7) could be observed near the blood vessels.

Evaluation of the antitumor effects *in vivo*

Free PTX, even at the highest dose tested (5 mg/kg) and non-targeted SF-NPs (containing 5 mg/kg of PTX), did not significantly inhibit tumor growth as compared to the vehicle-treated group (Figure 8A, $P>0.05$). The lower doses of the drug (1 or 2.5 mg/kg) were also ineffective (not shown). Targeted SF-NPs (containing 5 mg/kg of PTX) significantly inhibited tumor growth as compared to the vehicle, PTX, or non-targeted SF-NPs (Figure 8A, $P<0.05$, $P<0.01$, and $P<0.001$). Targeted SF-NPs inhibited tumor growth even at a lower dose (2.5 mg/kg) of the entrapped PTX (not shown). Similarly, targeted SF-NPs (containing 5 mg/kg of PTX) significantly the prolonged time of survival in tumor-bearing animals (Figure 8B, $P<0.01$ *vs.* the vehicle, free PTX (5 mg/kg), or non-targeted SF-NPs containing 5 mg/kg of PTX). Furthermore, targeted SF-NPs containing 2.5 mg/kg of PTX significantly repressed the growth of the tumor (not shown). Based on the histological evaluations, targeted SF-NPs containing 5 mg/kg of PTX induced remarkable tumor necrosis as compared to free PTX (5 mg/kg) or non-targeted SF-NPs containing 5 mg/kg of PTX (Figure 8C). Furthermore, no significant alterations in the morphology of the liver, heart, spleen, and kidney were observed (Figure 8C).

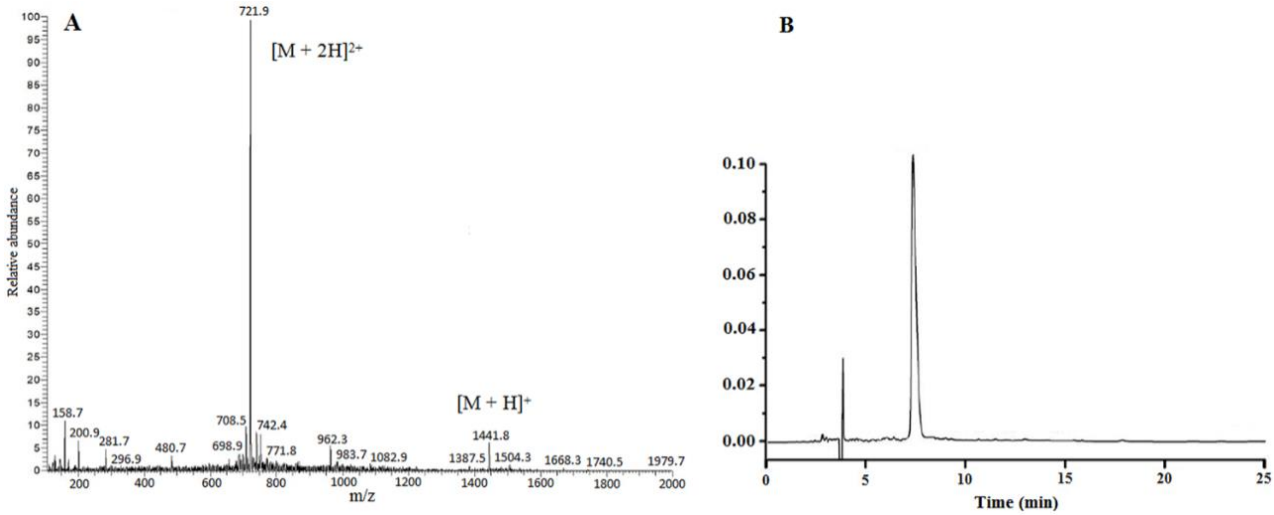

Figure 3. Electrospray ionization mass spectrum and HPLC profile of iRGD peptide. Mass spectrometry (A) confirmed the formation of the intra-molecular disulfide bond. m/z observed for [M + H]+ was 1441.8 that was in good agreement with the calculated mass (1441.5). HPLC profile of the peptide, including the retention time (8.6 min), has been demonstrated in part B. The synthesized peptide has shown a purity of about 98%

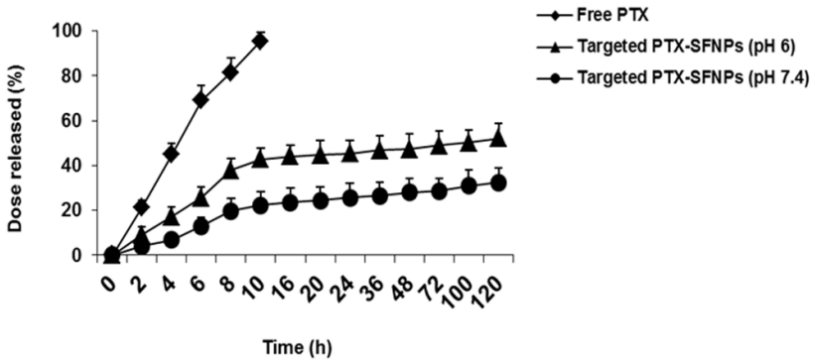

Figure 4. *In vitro* release pattern of PTX from targeted SF-NPs at physiological and acidic pH. PTX release from solution was more repaid than targeted PTX-SF-NPs formulation, which demonstrated a controlled release pattern. There was no remarkable difference between the kinetics of PTX released from NPs at physiological and acidic pH (P>0.05)

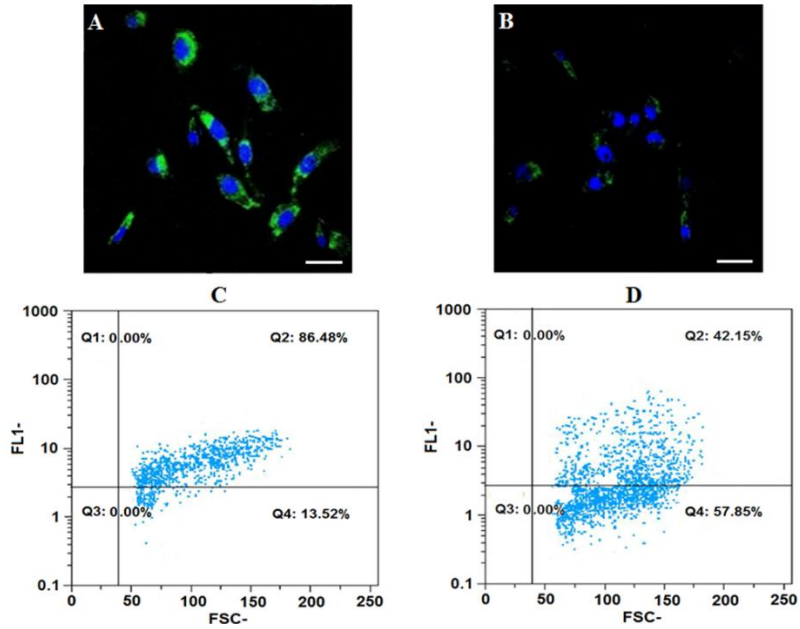

Figure 5. Confocal microscopic images and quantitative flow cytometric analysis of the cellular uptake of targeted (A and C) and non-targeted SF-NPs (B and D) into the MDA-MB-231 cells. (Scale bars: 50 µm)

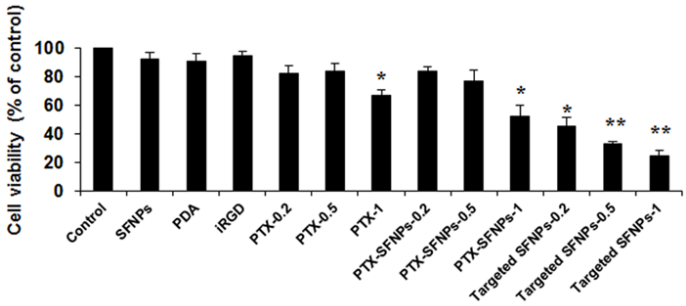

Figure 6. Assessment of the cytotoxicity *in vitro*. Using MTT assay for determining the viability of MDA-MB-231 breast cancer cells revealed dose-dependent cytotoxic effects of therapeutics. PTX and PTX-SF-NPs showed cytotoxic effects only at the highest dose of PTX (1 µM), while iRGD-PDA-PTX SF-NPs significantly reduced the cell viability at all doses tested. 0.2, 0.5, and 1 µM indicate the concentrations of free or encapsulated PTX in µM. Data are presented as mean±SEM (n=3). $^{*}P$<0.05, $^{**}P$<0.01 *vs.* the control group. (PTX: paclitaxel, SF-NPs: silk fibroin nanoparticles, Targeted SF-NPs: iRGD conjugated PDA-coated PTX-loaded SF-NPs)

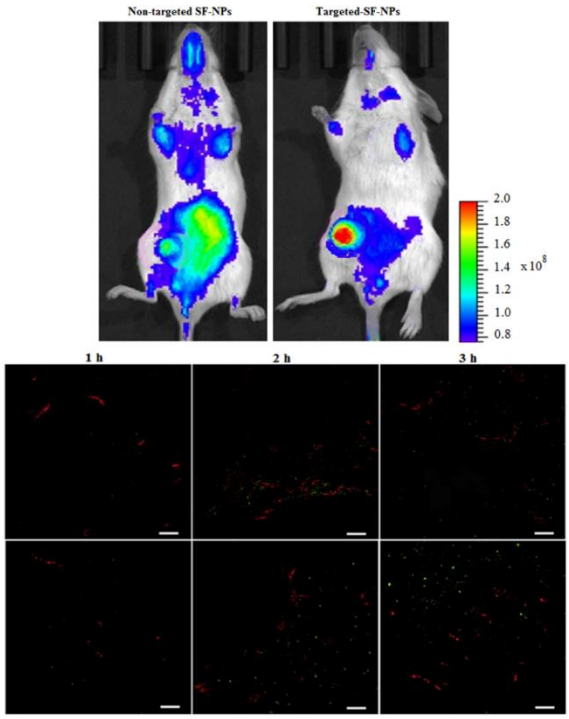

Figure 7. *In vivo* imaging of tumor-bearing animals three h after i.v. Injection of non-targeted or targeted SF-NPs and evaluation of their penetration into the tumor tissue. Fluorescence intensity in the tumor area of animals treated with targeted SF-NPs was remarkably stronger than that of non-targeted ones. Bar demonstrates the radiant efficiency ([p/sec/cm^2/sr] / [μW/cm^2]). Regarding the penetration of non-targeted (upper row) or targeted SF-NPs (lower row) into the tumor tissue, immunofluorescence staining revealed tumor accumulation of targeted NPs in a time-dependent fashion. Blood vessels and NPs can be observed in red and green, respectively. (Scale bar=50 μm)

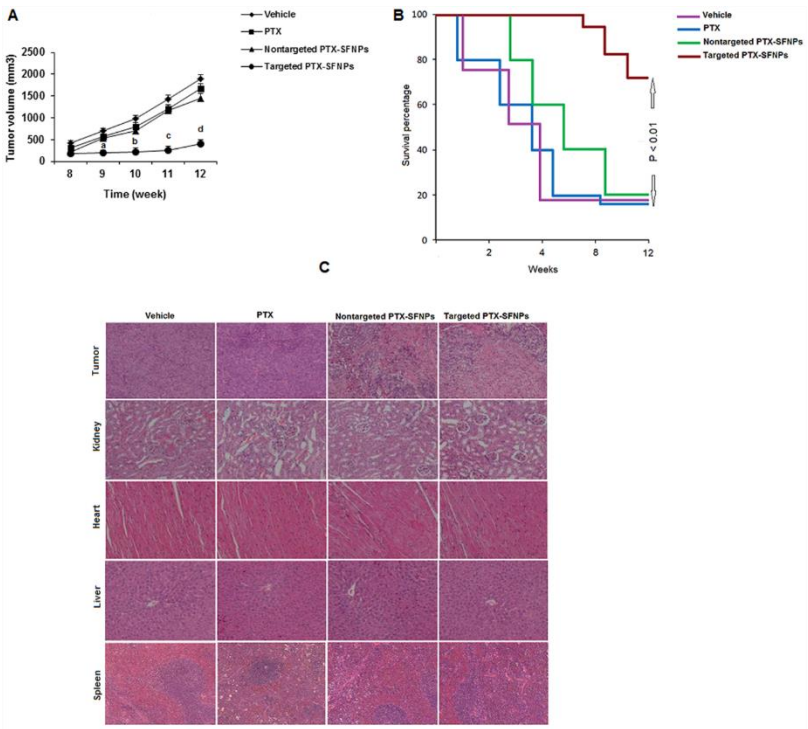

Figure 8. Therapeutic potential of the prepared SF-NPs against the breast tumor. iRGD-PDA-PTX-SFNPs (targeted SF-NPs containing 5 mg/kg of PTX) have shown promising antitumor effects, including reduced tumor growth, enhanced survival rate, and remarkable tumor necrosis while they have been safe towards the healthy organs. Free PTX or non-targeted SFNPs (at equivalent drug dose; 5 mg/kg) failed to exhibit significant antitumor effects. Data are given as mean±SEM (n=6). No considerable histological damage was observed in healthy organs (n=3)

Discussion

In the present study, we have developed iRGD-PDA-PTX-SF-NPs as a biomimetic nanoformulation against the breast cancer. Characterization of NPs including the morphological evaluation (Figure 1) demonstrated the appropriateness of the preparation method. Application of FTIR for assessment of the structural alterations of SF-NPs after drug loading, PDA coating, and peptide conjugation (Figure 2), indicated PTX loading in SF-NPs and successful PDA coating and iRGD conjugation. Evaluation of drug release profile demonstrated controlled release pattern (Figure 4). For mimicking the physiological condition and tumor microenvironment, the release profiles of PTX from SF-NPs were evaluated at pH values of 7.4 and 6 (Figure 4). As previously reported, the release of drugs from SF-NPs depends on the structure of silk as well as the interactions between silk and the drug (58). Faster drug release in the initial hours might be due to the higher PTX payload and presence of the entrapped drug at the hydrophilic-hydrophobic interface of SF-NPs. Accelerated drug release at acidic pH may be due to the weak interaction between the drug and SF-NPs. This type of release might be of therapeutic value, including the increased efficiency of the drug and reduced adverse effects against the healthy tissues. There was no significant difference between the kinetics of PTX release at physiological and acidic pH (Figure 4, $P>0.05$), suggesting the importance of using a suitable targeting agent onto the NPs.

For evaluating targeting ability of peptide-conjugated SF-NPs, the uptake behavior of NPs was investigated (Figure 5). As shown in Figure 5A, a significantly higher fluorescence was observed after incubation of MDA-MB-231 breast cancer cells with targeted SF-NPs as compared to the non-targeted ones (Figure 5B). This might be due to the high specificity of iRGD towards the integrins overexpressed on MDA-MB-231 cells. The findings were in good agreement with quantitative measurements of flow cytometry (Figure 5C and 5D) and represent targeted SF-NPs as suitable nanocarriers for increased drug uptake into the integrin-overexpressed cancer cells. This type of NPs may also be applied for recognizing the tumor cells.

Cytotoxicity evaluation revealed the biomimeticity of SF-NPs, PDA, and iRGD (Figure 6). Cytotoxic effects of targeted SF-NPs (iRGD-PDA-PTX-SF-NPs) even at the lower dose tested (Figure 6) might be of great significance for reducing the side effects of PTX. iRGD conjugation via improved interaction of SF-NPs with MDA-MB-231 cells and NPs internalization could facilitate the development of promising nanoplatforms for targeted drug delivery with minimal side effects.

In vivo imaging (Figure 7) demonstrated the significance of iRGD conjugation for targeted delivery and accumulation of drug at the tumor site that might result in the increased therapeutic efficiency and reduced side effects. Lower fluorescent intensities of non-targeted NPs throughout the body might be due to the non-selectivity of this type of NPs. Tumor penetration and accumulation of drug-loaded NPs are of great therapeutic significance. For further confirmation of NPs accumulation at the tumor site, immunofluorescence staining was performed. Figure 7 demonstrates distribution and tumor penetration of NPs in a time-dependent manner that might be due to the circulation of NPs followed by penetration into the tumor. The presence of non-targeted NPs near the blood vessels indicated lower tumor penetrability of this type of NPs (Figure 7). Following binding to αvβ3/αvβ5 integrins on the endothelial cells of the tumor, the peptide can spread within the tumor cells on which the similar integrins are expressed (59), leading to the superior penetrability of nanocarrier, increased drug efficiency, and reduced side effects.

Free PTX even at the highest dose tested and non-targeted SF-NPs did not remarkably inhibit tumor growth, while, targeted SF-NPs significantly inhibited tumor growth and prolonged survival time in tumor-bearing animals that might be due to higher penetrability and increased intra-tumoral accumulation of the drug (Figure 8). These findings demonstrate the efficiency of the prepared nanoformulation for improved intra-tumor penetration and accumulation of SF-NPs into the tumor leading to the prolonged lifetime of the cancer-affected animals and improved therapeutic index of the chemotherapeutic. Furthermore, targeted SF-NPs induced remarkable tumor necrosis, while, no remarkable alterations in the morphology of spleen, liver, kidney, and heart were observed indicating the safety of prepared NPs regarding the healthy organs. This may be due to the fact that integrins are not expressed in the normal tissues (60). Hence, a healthy organ could not be a target for iRGD-coupled NPs and their cytotoxic cargo. These findings indicate the superior potency and efficiency of iRGD-PDA-PTX-SFNPs nanoformulation that might be due to their enhanced tumor penetrability. Non-toxic effects of 5 mg/kg of PTX (Figure 8C) against the tumor might be

due to its inappropriate bioavailability, while controlled drug release from targeted SF-NPs and enhanced tumor penetrability induced promising antitumor effects. Noteworthy, tumor penetration of NPs may be associated with some limitations that may be due to the high interstitial-pressure of tumors (61,62). Increased iRGD accumulation in the tumor could increase the permeability of tumor vasculature leading to the improved antitumor activity of NP-based chemotherapeutics. iRGD-conjugated drugs or those co-administrated with the peptide can obtain higher anticancer efficiency because of the increased tumor penetrability (45). Tumor homing of iRGD usually occurs via binding to the integrins on the endothelium of tumor through the mediation of RGD motif and exposure of the binding motif to neuropilin-1 following the protease-induced bound cleavage leading to the increased cell or tissue penetration of NPs and their cargo delivery (63,64). Penetration of iRGD into the tumors has been suggested to occur via both vasculature- and circulation-independent fashions (45). Besides the expression of αv integrins, neuropilins (NRP-1, NRP-2) are highly expressed on the surface of tumor cells (60,65). iRGD has been shown to deeply spread within the tumor in energy- and NRP-1-dependent fashions (66). Excellent targeting ability of iRGD enables deep and effective penetration of various imaging or chemotherapeutic agents, polysomes, or immunomodulators leading to high-resolution imaging and increased antitumor efficiency, including metastasis therapy (63).

Besides preventing SF-NP aggregation, modification of SF-NP surface by PDA could facilitate the binding of biomolecules. Conjugation of PDA-coated SF-NPs with tumor-penetration enhancing peptide, iRGD, has provided a biomimetic nanoplatform for selective tumor targeting, enhanced permeability of tumor vasculature, and drug accumulation within the tumor leading to the remarkable suppression of tumor growth and prolonged time of survival due to the improved pharmacological profile of the entrapped drug. Reduced dose and dosage frequency might be associated with significantly reduced side effects and improved treatment outcomes.

References

1. Siegel RL, Miller KD, Jemal A. Cancer statistics, 2019. CA Cancer J Clin 2019;69:7-34.
2. Kassam F, Enright K, Dent R, Dranitsaris G, Myers J, Flynn C, et al. Survival outcomes for patients with metastatic triple-negative breast cancer: implications for clinical practice and trial design. Clin Breast Cancer 2009;9:29-33.
3. Anders CK, Carey LA. Biology, metastatic patterns, and treatment of patients with triple-negative breast cancer. Clin Breast Cancer 2009;9:S73-81.
4. Goldfarb Y, Ben-Eliyahu S. Surgery as a risk factor for breast cancer recurrence and metastasis: Mediating mechanisms and clinical prophylactic approaches. Breast Dis 2007;26:99-114.
5. McCubrey JA, Abrams SL, Fitzgerald TL, Cocco L, Martelli AM, Montalto G, et al. Roles of signaling pathways in drug resistance, cancer initiating cells and cancer progression and metastasis. Adv Biol Regul 2015;57:75-101.
6. Housman G, Byler S, Heerboth S, Lapinska K, Longacre M, Snyder N, et al. Drug Resistance in Cancer: An Overview. Cancers (Basel) 2014;6:1769-92.
7. Maribeth Maher. Current and Emerging Treatment Regimens for HER2-Positive Breast Cancer. P T 2014;39:206-12.
8. Shojaei S, Gardaneh M, Rahimi Shamabadi A. Target points in trastuzumab resistance. Int J Breast Cancer 2012;2012:761917.
9. Valabrega G, Montemurro F, Aglietta M. Trastuzumab: mechanism of action, resistance and future perspectives in HER2-overexpressing breast cancer. Ann Oncol 2007;18:977-84.
10. Reff ME, Hariharan K, Braslawsky G. Future of monoclonal antibodies in the treatment of hematologic malignancies. Cancer Control 2002;9:152-66.
11. Peer D, Karp JM, Hong S, Farokhzad OC, Margalit R, Langer R. Nanocarriers as an emerging platform for cancer therapy. Nat Nanotechnol 2007;2:751-60.
12. Ferrari M. Cancer nanotechnology: opportunities and challenges. Nat Rev Cancer 2005;5:161-71.
13. Toy R, Bauer L, Hoimes C, Ghaghada KB, Karathanasis E. Targeted nanotechnology for cancer imaging. Adv Drug Deliv Rev 2014; 76:79-97.
14. Shi J, Kantoff PW, Wooster R, Farokhzad OC. Cancer nanomedicine: progress, challenges and opportunities. Nat Rev Cancer 2017;17:20-37.
15. Cho K, Wang X, Nie S, Shin DM. Therapeutic Nanoparticles for Drug Delivery in Cancer. Clin. Cancer Res 2008;14:1310-6.
16. Patil YB, Toti US, Khdair A, Ma L, Panyam J. Single-Step Surface Functionalization of Polymeric Nanoparticles for Targeted Drug Delivery. Biomaterials 2009;30:859-66.
17. Leal-Egaña A, Scheibel T. Silk-based materials for biomedical applications. Biotechnol Appl Biochem 2010;55:155-67.

18. Wang Y, Blasioli DJ, Kim HJ, Kim HS, Kaplan DL. Cartilage tissue engineering with silk scaffolds and human articular chondrocytes. Biomaterials 2006;27:4434-42.
19. Omenetto FG, Kaplan DL. New opportunities for an ancient material. Science 2010;329:528-31.
20. Heim M, Keerl D, Scheibel T. Spider silk: from soluble proteinto extraordinary fiber. Angew Chem Int Ed Engl 2009;48:3584-96.
21. Zheng Z, Li Y, Xie MB. Silk Fibroin-Based Nanoparticles for Drug Delivery. Int J Mol Sci 2015;16:4880-903.
22. Kundu J, Chung YI, Kim YH, Tae G, Kundu SC. Silk fibroin nanoparticles for cellular uptake and control release. Int J Pharm 2010;388:242-50.
23. Yucel T, Lovett ML, Giangregorio R, Coonahan E, Kaplan DL. Silk fibroin rods for sustained delivery of breast cancer therapeutics. Biomaterials 2014;35:8613-20.
24. Wu P, Liu Q, Li R, Wang J, Zhen X, Yue G, et al. Facile preparation of paclitaxel loaded silk fibroin nanoparticles for enhanced antitumor efficacy by loco-regional drug delivery. ACS Appl Mater Interfaces 2013;5:12638-45.
25. Seib FP, Jones GT, Rnjak-Kovacina J, Lin Y, Kaplan DL. pH-dependent anticancer drug release from silk nanoparticles. Adv Healthc Mater 2013;2:1606-11.
26. Subia B, Kundu SC. Drug loading and release on tumor cells using silk fibroin-albumin nanoparticles as carriers. Nanotechnology 2013;24:035103.
27. Hassanzadeh P, Arbabi E, Rostami F. Lipid-based nanocarriers provide prolonged anticancer activity for palbociclib: *In vitro* and *in vivo* evaluations. Acta Med Iran 2021;59:87-93.
28. Lin Z, Gao W, Hu H, Ma K, He B, Dai W, et al. Novel thermo-sensitive hydrogel system with paclitaxel nanocrystals: High drug-loading, sustained drug release and extended local retention guaranteeing better efficacy and lower toxicity. J Control Release 2014;174:161-70.
29. Zhang L, He Y, Ma G, Song C, Sun H. Paclitaxel-loaded polymeric micelles based on poly(ε-caprolactone)-poly(ethylene glycol)-poly(ε-caprolactone) triblock copolymers: in vitro and in vivo evaluation. Nanomedicine 2012;8:925-34.
30. Vepari C, Kaplan DL. Silk as a biomaterial. Prog Polym Sci 2007;32:991-1007.
31. Murphy AR, Kaplan DL. Biomedical applications of chemically-modified silk fibroin. J Mater Chem 2009;19:6443-50.
32. Ishihara T, Maeda T, Sakamoto H, Takasaki N, Shigyo M, Ishida T, et al. Evasion of the accelerated blood clearance phenomenon by coating of nanoparticles with various hydrophilic polymers. Biomacromolecules 2010;11:2700-6.
33. Wang X, Ishida T, Kiwada H. Anti-PEG IgM elicited by injection of liposomes is involved in the enhanced blood clearance of a subsequent dose of PEGylated liposomes. J Control Release 2007;119:236-44.
34. Hoang B, Lee H, Reilly RM, Allen C. Noninvasive monitoring of the fate of 111In-labeled block copolymer micelles by high resolution and high sensitivity MicroSPECT/CT imaging. Mol Pharm 2009;6:581-92.
35. Xu H, Wang KQ, Deng YH, Chen DW. Effects of cleavable PEG-cholesterol derivatives on the accelerated blood clearance of PEGylated liposomes. Biomaterials 2010;31:4757-63.
36. Yan P, Wang J, Wang L, Liu B, Lei Z, Yang S. The in vitro Biomineralization and Cytocompatibility of Polydopamine Coated Carbon Nanotubes. Appl Surf Sci 2011;257:4849-55.
37. Zheng QS, Lin T, Wu H, Guo L, Ye P, Hao Y, et al. Mussel-inspired polydopamine coated mesoporous silica nanoparticles as pH-sensitive nanocarriers for controlled release. Int J Pharm 2014;463:22-6.
38. Liu Y, Ai K, Lu L. Polydopamine and its derivative materials: synthesis and promising applications in energy, environmental, and biomedical fields. Chem Rev 2014;114:5057-115.
39. Ho CC, Ding SJ. Structure, properties and applications of mussel-inspired polydopamine. J Biomed Nanotechnol 2014;10:3063-84.
40. Hassanzadeh P, Arbabi E, Rostami F. Development of a novel nanoformulation against the colorectal cancer. Life Sci 2021;281:119772.
41. Sun H, Dong Y, Feijen J, Zhong Z. Peptide-decorated polymeric nanomedicines for precision cancer therapy. J Control Release 2018;290:11-27.
42. Wanjale MV, Kumar GSV. Peptides as a therapeutic avenue for nanocarrier-aided targeting of glioma. Expert Opin Drug Deliv Expert Opin Drug Deliv 2017;14:811-24.
43. Komin A, Russell LM, Hristova KA, Searson PC. Peptide-based strategies for enhanced cell uptake, transcellular transport, and circulation: mechanisms and challenges. Adv Drug Deliv Rev 2017;110-111:52-64.
44. Peng M, Qin S, Jia H, Zheng D, Rong L, Zhang X. Self delivery of a Peptide-Based Prodrug for Tumor-Targeting Therapy. Nano Res 2016;9:663-73.
45. Sugahara KN, Teesalu T, Karmali PP, Kotamraju VR, Agemy L, Greenwald DR, et al. Coadministration of a tumor-penetrating peptide enhances the efficacy of cancer drugs. Science 2010;328:1031-5.
46. Ruoslahti E. Tumor penetrating peptides for improved drug delivery. Adv Drug Deliv Rev 2017;110-1:3-12.

47. Ruoslahti E. Access granted: iRGD helps silicasome-encased drugs breach the tumor barrier. J Clin Invest 2017;127:1622-4.
48. Rockwood DN, Preda RC, Yucel T, Wang X, Lovett ML, Kaplan DL. Materials Fabrication From Bombyx Mori Silk Fibroin. Nat Protoc 2011;6:1612-31.
49. Yu Zhang, Yixin Zhong, Man Ye, Jie Xu, Jia Liu, Jun Zhou, et al. Polydopamine-modified dual-ligand nanoparticles as highly effective and targeted magnetic resonance/photoacoustic dual-modality thrombus imaging agents. Int J Nanomedicine 2019:14;7155-71.
50. Cho HJ, Lee SJ, Park SJ, Paik CH, Leed SM, Kim S, et al. Activatable iRGD-based peptide monolith: targeting, internalization, and fluorescence activation for precise tumor imaging. J Control Release 2016;237:177-84.
51. Kotamraju VR, Sharma S, Kolhar P, Agemy L, Pavlovich J, Ruoslahti E. Increasing Tumor Accessibility with Conjugatable Disulfide-Bridged Tumor-Penetrating Peptides for Cancer Diagnosis and Treatment. Breast Cancer (Auckl) 2016;9:79-87.
52. Pan G, Sun S, Zhang W, Zhao R, Cui W, He F, et al. Biomimetic Design of Mussel-Derived Bioactive Peptides for Dual-Functionalization of Titanium-Based Biomaterials. J Am Chem Soc 2016;138:15078-86.
53. Karmali PP, Kotamraju VR, Kastantin M, Black M, Missirlis D, Tirrell M, et al. Targeting of albumin-embedded paclitaxel nanoparticles to tumors. Nanomedicine 2009;5:73-82.
54. Zhu S, Qian L, Hong M, Zhang L, Pei Y, Jiang Y. RGD-modified PEG-PAMAMDOX conjugate: in vitro and in vivo targeting to both tumor neovascular endothelial cells and tumor cells. Adv Mater 2011;23:H84e9.
55. Danhier F, Lecouturier N, Vroman B, Jérôme C, Marchand-Brynaert J, Feron O, et al. Paclitaxel-loaded PEGylated PLGA-based nanoparticles: In vitro and in vivo evaluation. J Control Release 2009;133:11-7.
56. Qifan W, Fen N, Ying X, Xinwei F, Jun D, Ge Z. iRGD-targeted delivery of a pro-apoptotic peptide activated by cathepsin B inhibits tumor growth and metastasis in mice. Tumour Biol 2016;37:10643-52.
57. Carmichael J, DeGraff WG, Gazdar AF, Minna JD, Mitchell JB. Evaluation of a tetrazolium-based semiautomated colorimetric assay: assessment of chemosensitivity testing. Cancer Res 1987;47:936-41.
58. Lammel A, Xiao H, Park SH, Kaplan DL, Scheibel TR. Controlling silk fibroin particle features for drug delivery. Biomaterials 2010;31:4583-91.
59. Teesalu T, Sugahara KN, Kotamraju VR, Ruoslahti E. C-end rule peptides mediate neuropilin-1-dependent cell, vascular, and tissue penetration. Proc Natl Acad Sci U S A 2009;106:16157-62.
60. Desgrosellier JS, Cheresh DA. Integrins in cancer: biological implications and therapeutic opportunities. Nat Rev Cancer 2010;10:9-22.
61. Jain RK. Vascular and interstitial barriers to delivery of therapeutic agents in tumors. Cancer Metastasis Rev 1990;9:253-66.
62. Heldin CH, Rubin K, Pietras K, Ostman A. High interstitial fluid pressure - an obstacle in cancer therapy. Nat Rev Cancer 2004;4:806-13.
63. Zuo H. iRGD: A Promising Peptide for Cancer Imaging and a Potential Therapeutic Agent for Various Cancers. J Oncol 2019;2019:9367845.
64. Xiangsheng Liu, Andre E. Nel, Huan Meng. Tumor-penetrating peptide enhances transcytosis of silicasome-based chemotherapy for pancreatic cancer. J Clin Invest 2017;127:1622-4.
65. Prud'homme GJ, Glinka Y. Neuropilins are multifunctional coreceptors involved in tumor initiation, growth, metastasis and immunity. Oncotarget 2012;3:921-39.
66. Chen R, Braun GB, Luo X, Sugahara KN, Teesalu T, Ruoslahti E. application of a proapoptotic peptide to intratumorally spreading cancer therapy. Cancer Res 2013;73:1352-61.